Supplementary Material to Mas e Braga et al. "Nunataks as barriers to ice flow: implications for palaeo ice-sheet reconstructions"

Compilation of sample position relative to ice flow

For Figs. 2 and S9, we compile [10]Be and ^{14}C exposure ages in Antarctica, and show how they position from the nunatak summit differs from the direction of ice flow at the nunatak surroundings. Boulder samples containing [10]Be ages were extracted from the expage compilation, by Jakob Heyman (https://expage.github.io/data.html last accessed: March 19th, 2021), considering the "published" ages. Samples containing ^{14}C ages were extracted from the Ice-D database (http://antarctica.ice-d.org/ last accessed: April 30th, 2021), considering those calculated with the LSDn scaling method. The ^{14}C ages dataset includes the following publications: Balco et al. (2016), Johnson et al. (2019, 2020), Goehring et al. (2019), Nichols et al. (2019). For both datasets, a sample's position vector (**P**) was calculated relative to the closest nunatak summit. The summits were extracted from BedMachine Antarctica (Morlighem et al., 2020) by calculating the Topographic Position Index (TPI, Wilson et al, 2007), which yields only the most prominent features, removes noise, and allows a faster computation time of the raster calculations. A morphological feature map (Wood, 1996) was created from the TPI map, considering slopes steeper than 5° within a processing window of 5 grid points. The orientation of **P** was compared to the orientation of ice-flow in the closest vicinity of the nunatak (**F**). The ice-flow vectors were extracted from the Measures 20 km dataset in Quantarctica v3.2 (Matsuoka et al., 2021), and they indicate regional ice flow directions, rather than local. We use polar histograms to plot the offset between **P** and **F** (i.e., **O** = **P** – **F**).

In this compilation, we refrained from filtering for sample distance from the summit. We first considered samples within 30 km of the summit, but found that the number of statistically significant results was considerably smaller. We divided the data into four sectors that span a 90° arc each: downstream face, upstream face, and two flanks. We tested the use of narrower sectors (45° as opposed to 90°) for classifying a sample, but this also yielded too few samples. To minimise the effect of inheritance, we restricted [10]Be and ^{14}C samples to those with exposure ages younger than 20 ka. In the ^{14}C dataset, samples with multiple measurements have their age and uncertainties represented as the mean of all measurements.

Compilation of the nunatak dataset

Several profiles of nunataks along the ice flow were taken in order to constrain the obstacle dimensions used in our experiments (Fig. S1). The chosen nunataks include examples of different areas of the Antarctic continent where they are present (Fig. S2), and were selected so that they would be at least 50 km apart from other major obstacles along flow. More examples were taken from Dronning Maud Land due to the strong relief and higher nunatak availability. To determine the axis lengths of the Gaussian surface used, nunatak axis lengths were determined by fitting an ellipse around the exposed part of the nunatak, and taking the lengths of its major and minor axes. Similarly, outlet-glacier width was compiled by analysing the spacing between nunataks in nunatak ranges at the same locations. Figure S3 shows the frequency distribution for major and minor axes, and the distribution of outlet-glacier width. Our major axis size lies at the upper end of the most common nunataks observed, and the remaining values used for these three variables in our model experiments cover 80 – 90 % of the typical sizes. Finally, we consider the three-nunatak 0 km-spacing experiment to satisfactorily cover the largest nunatak cases.
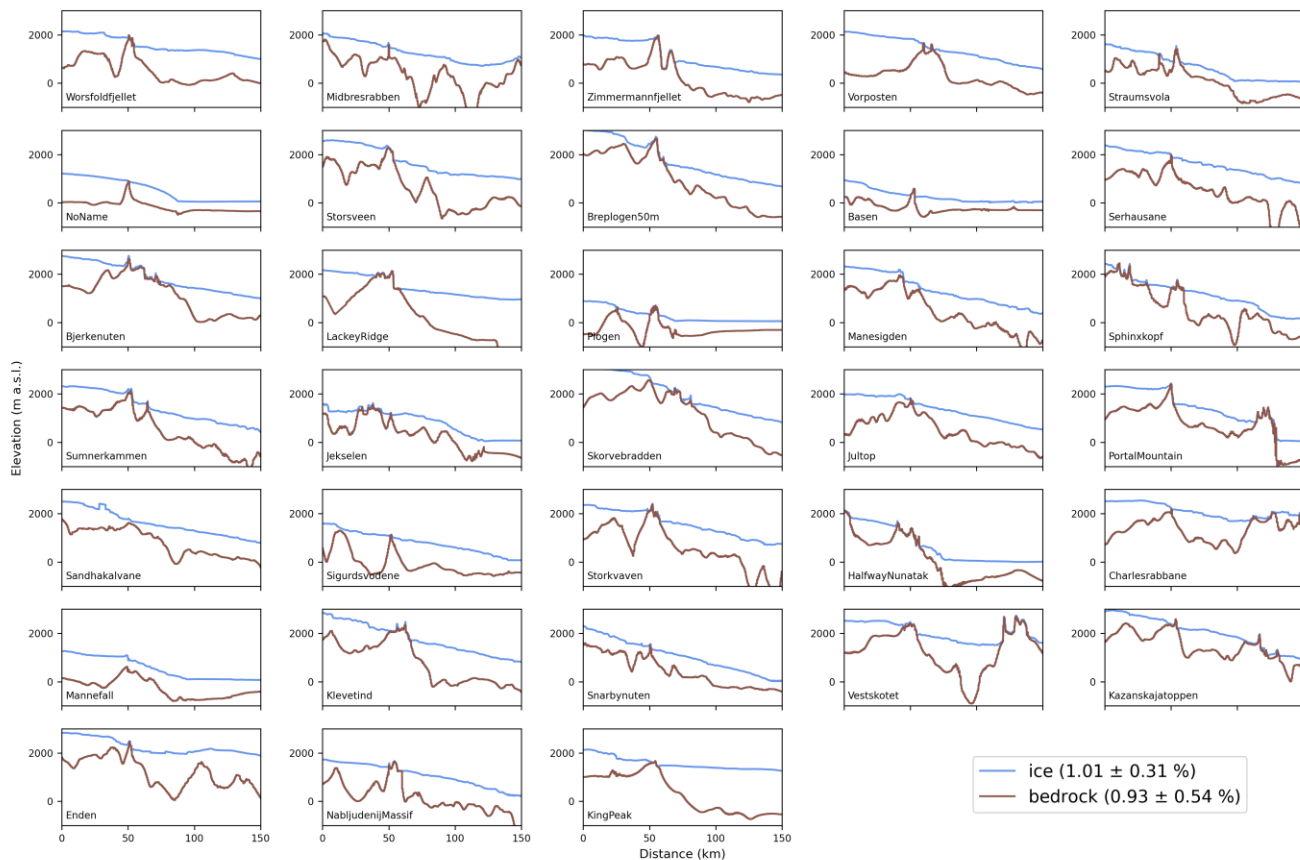
Figure S1. Along-stream nunatak profiles showing ice surface (blue; Howat et al., 2019) and bedrock (brown; Morlighem et al., 2019) for 33 nunataks distributed around the Antarctic continent (Fig. S2). Profiles were taken 50 km upstream and 100 km downstream of the nunatak's summit. Legend shows the average inclination of the ice surface and bedrock for all the profiles. Nunatak naming follows the Scientific Committee for Antarctic Research (SCAR) gazeteer (https://www.scar.org/data-products/place-names/; last accessed on January 21st, 2021).
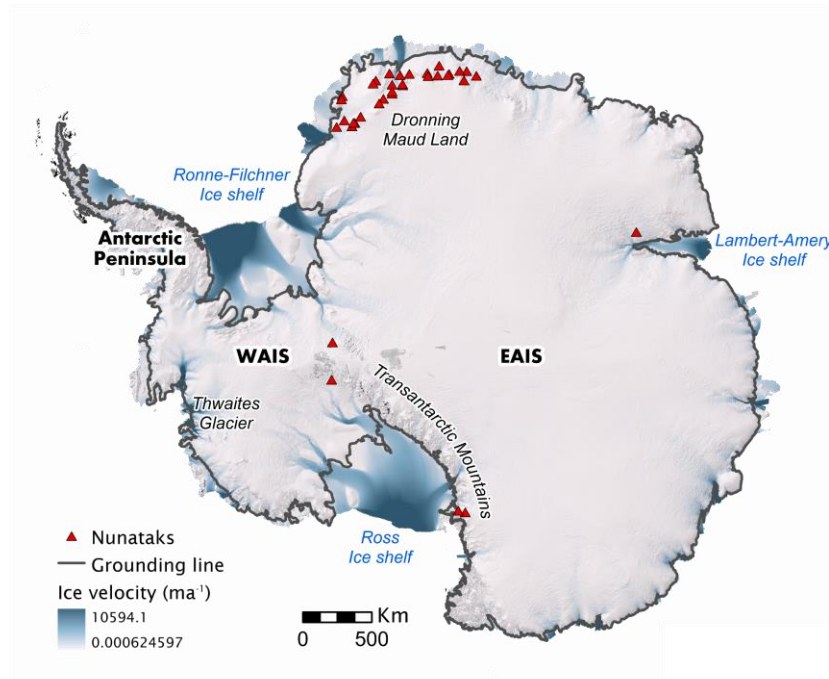
Figure S2. Distribution around the Antarctic continent of the nunataks shown in Fig. S1 (red triangles) superimposed on
60   ice-surface height (Howat et al., 2019; shading). Blue colours show ice surface velocity (Mouginot et al., 2012), and black
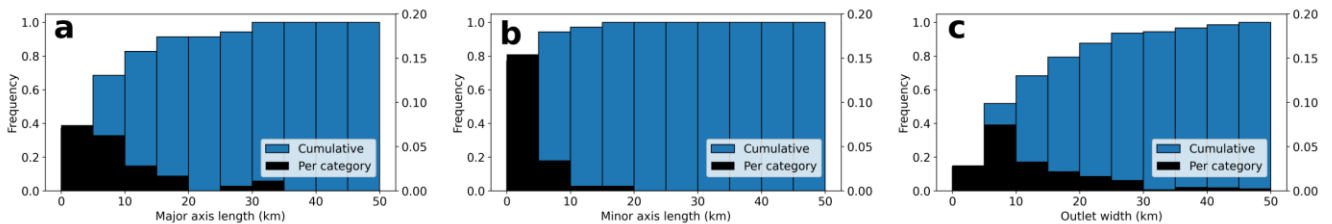line denotes the corresponding grounding line.

65

Figure S3. Histograms of the distribution (per category and cumulative) of nunatak characteristics used in defining the
experimental design: (a) major, (b) minor axis lengths, and (c) outlet-glacier width flanking the nunataks shown in Figs. S1
and S2. Black bars (right y axis) show the distribution per category, and blue bars (left y axis) show the cumulative
distribution.

70

Sensitivity of the ice surface evolution to end-member parameter choices

75   In order to assess the robustness of our results relative to the choice of model parameters, namely *C*,
which controls basal sliding in Weertman's flow law, and *A*, which controls the ice rheology in Glen's
flow law, we repeated the 'thw' experiment using other possible choices of model parameters. These
were also based on the distribution maps for A and C in Gudmundsson et al. (2019), focusing on areas
of strong topographic relief around nunataks. The parameter space covered in these sensitivity tests are
80   T = -5 °C and T = -10 °C for the ice temperature influence on A, and $\log_{10}(C) = -3.5$ and $\log_{10}(C) = -5.5$

for basal sliding. We chose the nunatak elongated transverse to flow for these experiments because its shape was shown to yield the strongest ice-surface response compared with the nunatak elongated parallel to flow.

85 Overall, the setup was rather insensitive to the adopted temperature, since results using -5 and -10 ºC yield similar results close to the nunataks (Fig. S4). Temperature played a much stronger role in the position of the grounding line, which is beyond the region of interest of our study. Conversely, the ice cap configuration was more sensitive to the choice of basal slipperiness (Fig. S5). Choosing a higher sliding parameter yielded a much thinner ice cap, and surface velocities were twice as high as in the
90 control run. When prescribing higher friction (i.e., less sliding) at the bed, the resulting ice cap was much thicker, and did not have a floating-ice terminus. The increased driving stress caused by the thicker ice resulted in mean (median) surface velocities similar to the control run: 32 (30) ma^{-1}, compared to 33 (29) ma^{-1}, but slower maximum velocities at the nunatak flanks (39 compared to 53 ma^{-1}).
95 The choice of parameters used in the experiments presented in the main text (treated here as 'control') were shown to yield a profile that is a better generalisation of the profiles in Fig. S1. In the higher sliding case (Fig. S5a), the ice becomes too thin after the spin up, and consequently would yield an almost ice-free domain after the thinning experiments. In the lower sliding case (Fig. S5b), flow velocity at the nunatak flanks s still within the range of values observed along the nunatak profiles (Fig.
100 2e in the main text), and the absence of a floating terminus would require a higher ablation to perform marine ice sheet instability experiments. While these are still plausible conditions for our setup, the resulting surface slope of 1.7% is almost 50% steeper than the control run (1.3%), which is already at the upper end of the range of values observed for Antarctic nunataks (Fig. S1).
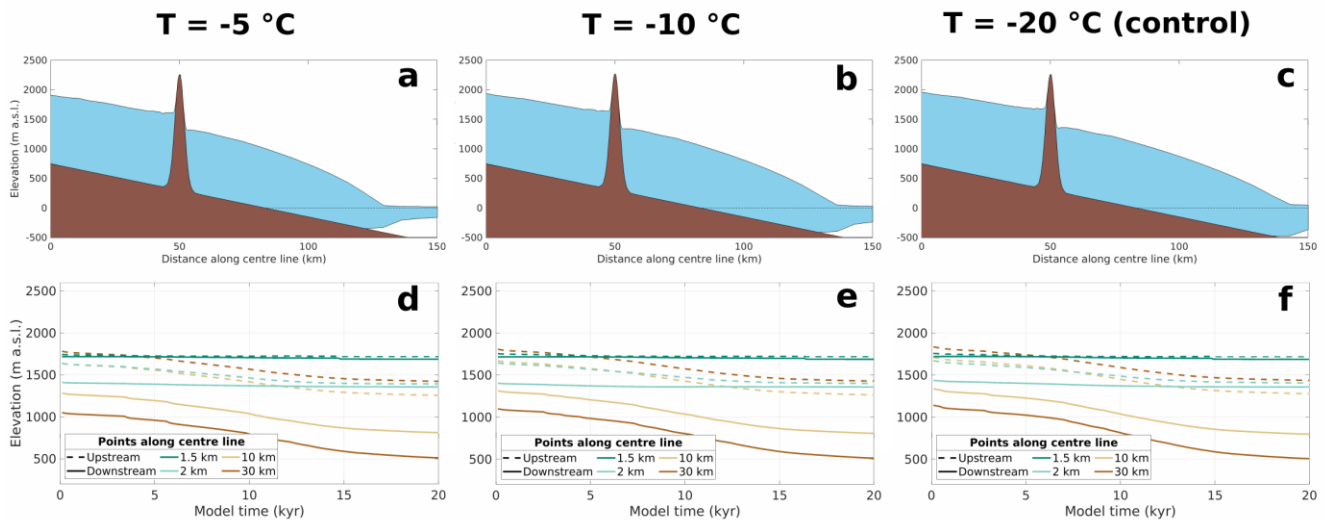

105

Figure S4. Sensitivity experiments for the ice rheology factor (A), where the value for ice temperature used in Glen's flow law is varied. Values tested were -5 (a,d), -10 (b,e) and -20 ºC (control, as in the main experiments; c,f). Upper panels show the post-spin up transect at the centre line (as in Fig. 2c of the main text), while lower panels show the ice surface evolution at select points away from the nunatak (as in Figs. 3b,d of the main text).

110
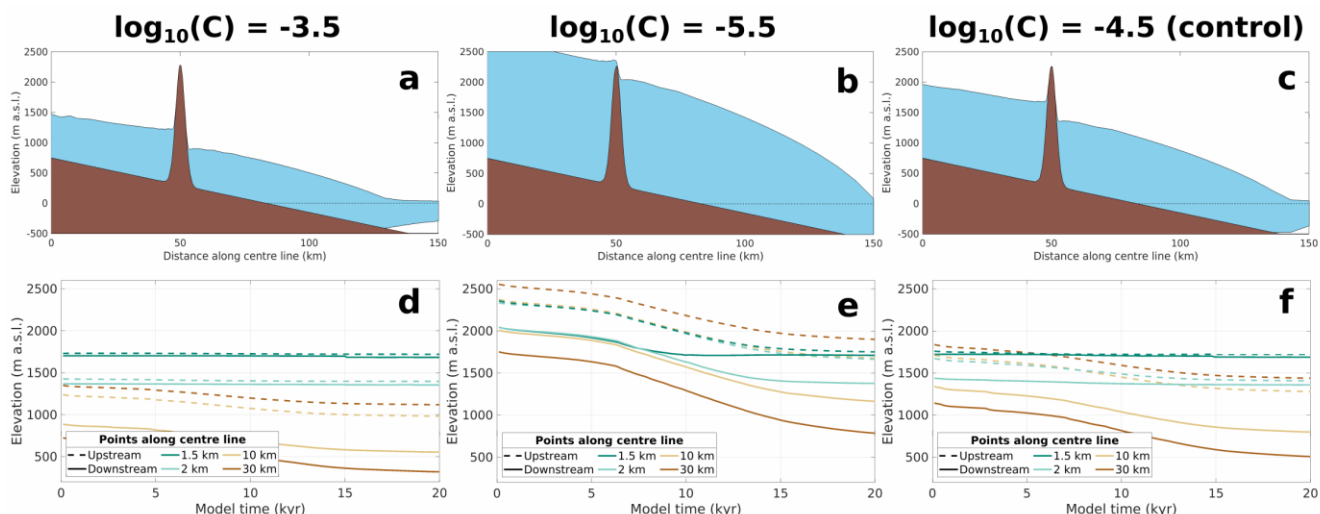
Figure S5. Sensitivity experiments for ice rheology, where the value for basal slipperiness (C) used in Weertman's sliding law is varied. Values tested were $\log_{10}(C)$ = -3.5 (a,d), -5.5 (b,e) and -4.5 (control, as in the main experiments; c,f). Upper panels show the post-spin up transect at the centre line (as in Fig. 2c of the main text), while lower panels show the ice surface evolution at select points away from the nunatak (as in Figs. 3b,d of the main text).
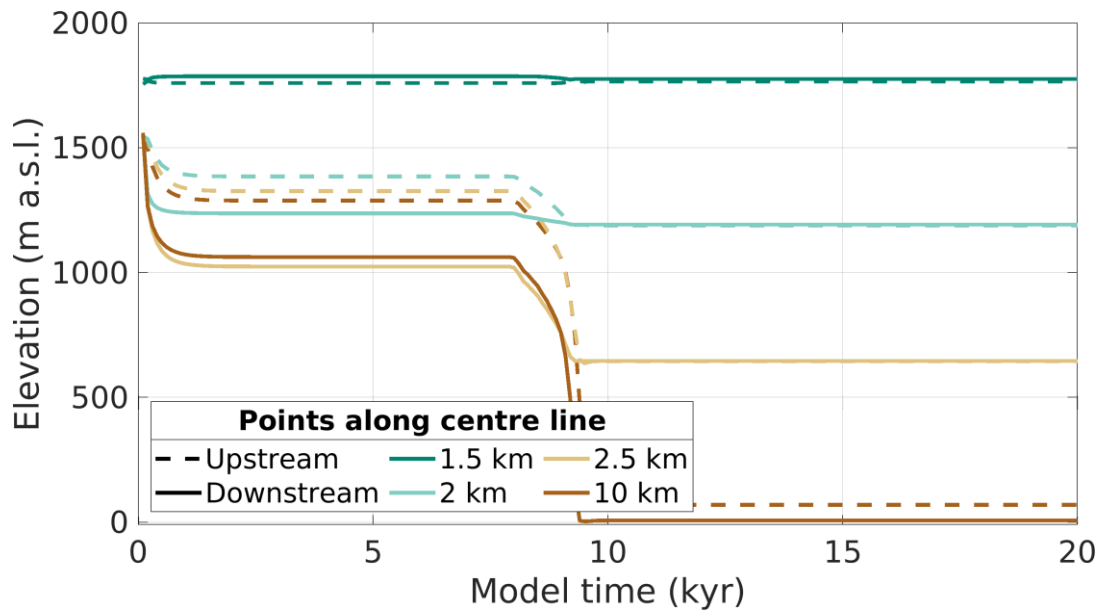
Other supplementary figures
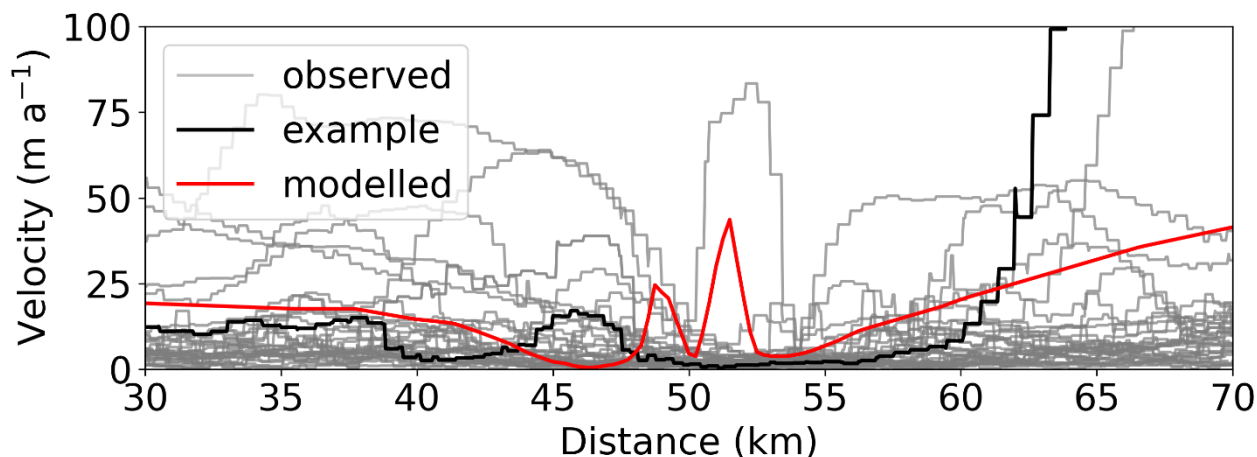
Figure S6. Surface velocity profiles across 33 nunataks (grey, observed; black line refers to the example profile in d; Mouginot et al., 2012) and along the spun-up ice cap centreline (red, modelled); only the first 20 km up and downstream of the nunatak are shown for a better visualisation (nunatak summits are centred on x=50 km).

Figure S7. Surface evolution of select points equidistant (up and downstream) from the nunatak centre along the domain centre line, for an experiment on a retrograde bed slope (cf. Methods section in the main text).
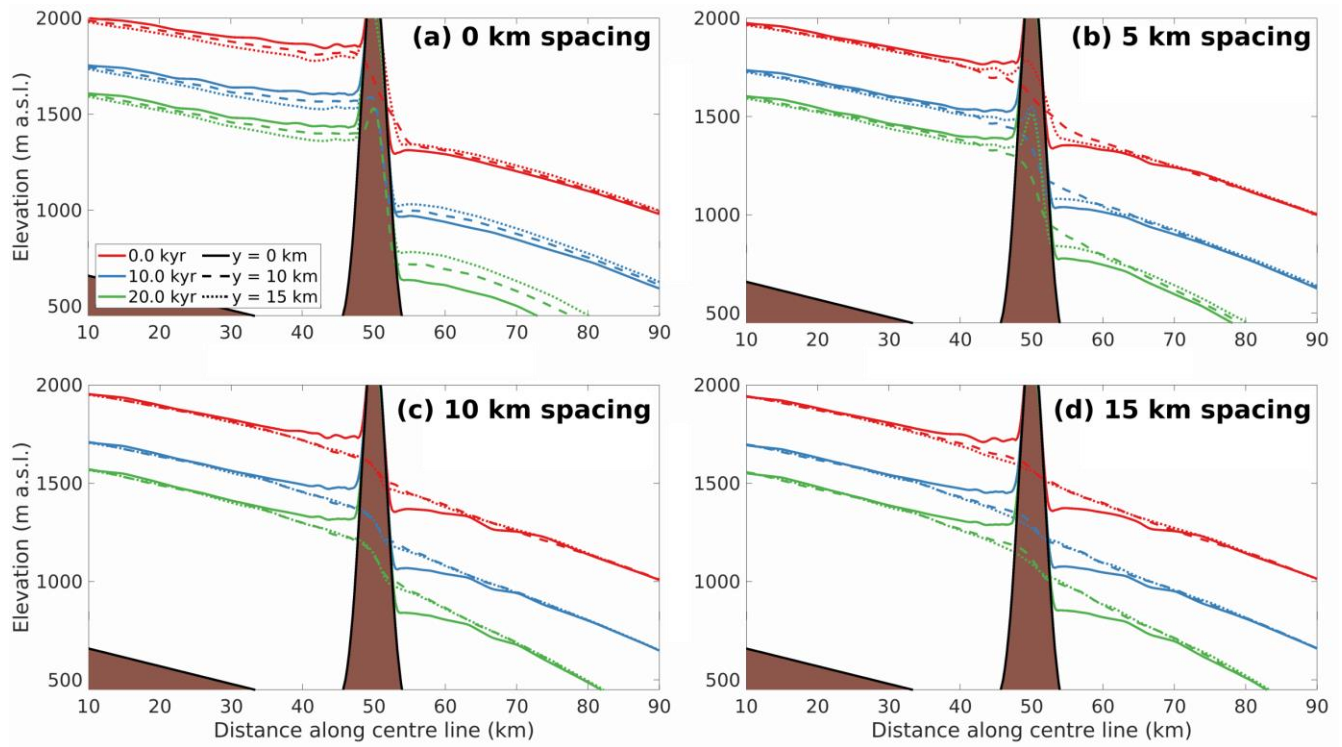
Figure S8. Ice-surface Isochrones (as in Figs. 3 and 7 of the main text), but for the different three-nunatak experiments, where the spacing between them is (a) 0 km, (b) 5 km, (c) 10 km, (d) 15 km.
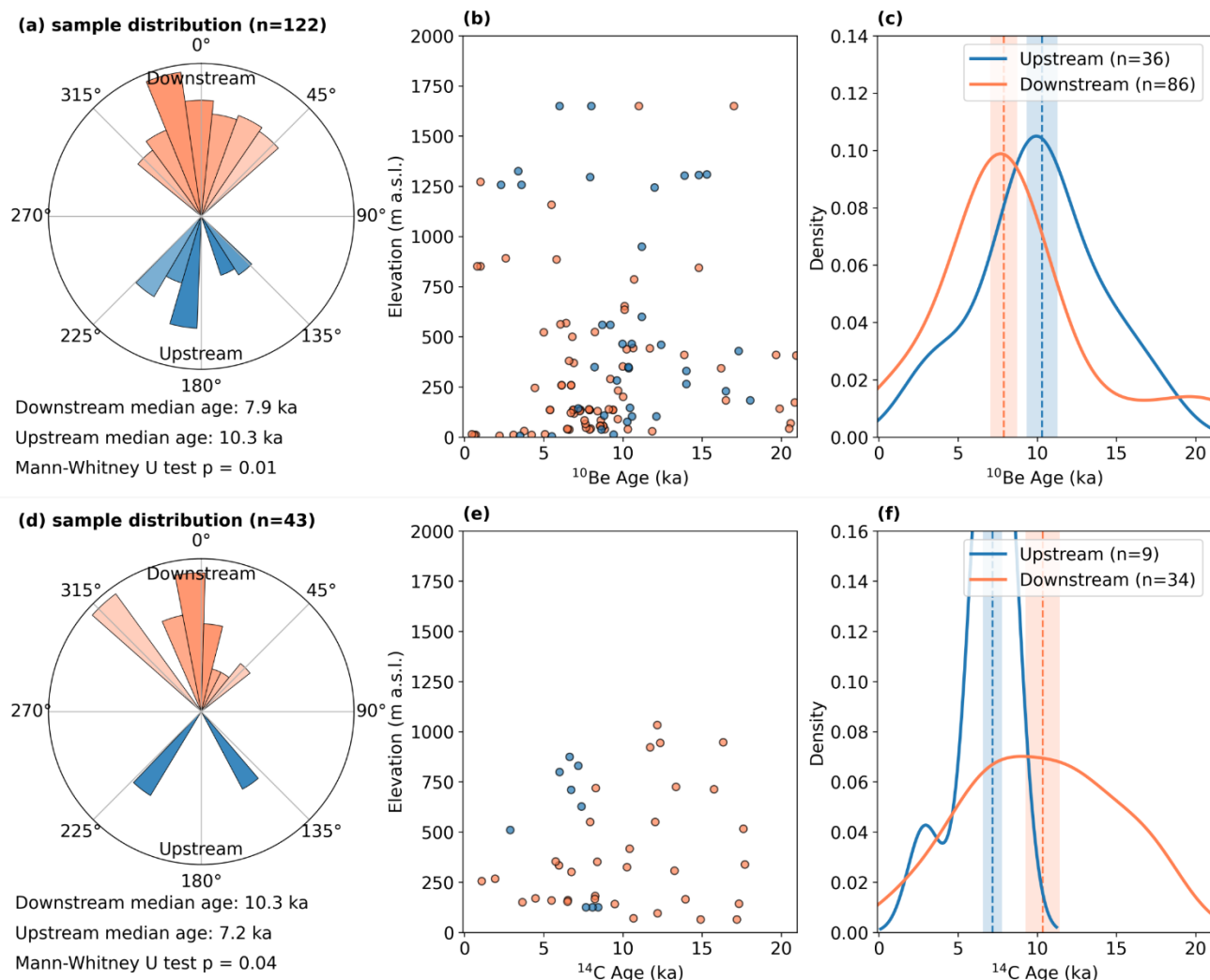
Figure S9. Relationship between exposure-age samples and ice flow in Antarctica. Panels a – c show post-Last Glacial Maximum ^{10}Be ages, and panels d – f show post-Last Glacial Maximum ^{14}C ages. (a,d) Polar histogram as in Fig. 2 of the main text, but restricted to the up and downstream faces of the nunatak (i.e., between 315º and 45º downstream, and 135º and 225º upstream). (b,e) Relationship between sample elevation above sea level (m a.s.l.) and published ^{10}Be/calculated ^{14}C exposure ages (in thousand years ago, ka) for the samples that compose panels a and d, respectively. (c,f) kernel density function of the ages shown in panels b and e, respectively. In these plots, the dashed line shows the median age, and the shading shows the uncertainty interval based on the median uncertainty in ^{10}Be ages, and median external error in ^{14}C ages. The median ages for each sample group are also displayed, along with the p value for the two-sided Mann-Whitney U test.

References

155   Balco G, Todd C, Huybers K, Campbell S, Vermeulen M, Hegland M, Goehring BM, Hillebrand TR. (2016) Cosmogenic-nuclide exposure ages from the Pensacola Mountains adjacent to the Foundation Ice Stream, Antarctica. *American Journal of Science* v. 316(6), 542-77. doi: https://doi.org/10.2475/06.2016.02

Goehring BM, Balco G, Todd C, Moening-Swanson I, Nichols K. (2019) Late-glacial grounding line retreat in the northern Ross Sea, Antarctica. *Geology* v. 47(4), 291–294. doi: https://doi.org/10.1130/G45413.1

160

Gudmundsson, G. H., Paolo, F. S., Adusumilli, S., and Fricker, H. A.: Instantaneous Antarctic ice sheet mass loss driven by thinning ice shelves, Geophysical Research Letters, 46, 13 903–13 909, 2019.

Howat, I. M., Porter, C., Smith, B. E., Noh, M.-J., and Morin, P.: The Reference Elevation Model of Antarctica, The
165   Cryosphere, 13, 665–674, 2019.

Johnson JS, Roberts SJ, Rood DH, Pollard D, Schaefer JM, Whitehouse PL, Ireland LC, Lamp JL, Goehring BM, Rand C, Smith JA. Deglaciation of Pope Glacier implies widespread early Holocene ice sheet thinning in the Amundsen Sea sector of Antarctica. (2020) *Earth and planetary science letters* v. 548, 116501. doi: https://doi.org/10.1016/j.epsl.2020.116501

170

Johnson JS, Nichols KA, Goehring BM, Balco G, Schaefer JM. Abrupt mid-Holocene ice loss in the western Weddell Sea Embayment of Antarctica. (2019) *Earth and Planetary Science Letters* v. 518, 127-35. doi: https://doi.org/10.1016/j.epsl.2019.05.002

175   Morlighem, M., Rignot, E., Binder, T., Blankenship, D., Drews, R., Eagles, G., Eisen, O., Ferraccioli, F., Forsberg, R., Fretwell, P., et al.: Deep glacial troughs and stabilizing ridges unveiled beneath the margins of the Antarctic ice sheet, Nature Geoscience, 13, 132–137, 2020.

Mouginot, J., Scheuchl, B., and Rignot, E.: Mapping of ice motion in Antarctica using synthetic-aperture radar data, Remote
180   Sensing, 4,2753–2767, 2012.

Nichols KA, Goehring BM, Balco G, Johnson JS, Hein AS, Todd C. New Last Glacial Maximum ice thickness constraints for the Weddell Sea Embayment, Antarctica. (2019) The Cryosphere v. 13(11), 2935-2951. doi: https://doi.org/10.5194/tc-13-2935-2019

185

Wilson MF, O'Connell B, Brown C, Guinan JC, Grehan AJ. Multiscale terrain analysis of multibeam bathymetry data for habitat mapping on the continental slope. (2007) Marine Geodesy v. 30(1-2), 3-5. https://doi.org/10.1080/01490410701295962

190   Wood, J. 1996. The Geomorphological Characterisation of Digital Elevation Models.. Ph.D. Thesis, University of Leicester. http://hdl.handle.net/2381/34503